

## MILDLY-COMPRESSIBLE PRESSURE-BASED CFD METHODOLOGY FOR ACOUSTIC PROPAGATION AND ABSORPTION PREDICTION

**B. Gunasekaran and J. J. McGuirk**  
Dept. of Aero. & Auto. Eng., Loughborough Univ.,  
Loughborough, Leicestershire. LE11 3TU, UK.

### ABSTRACT

A modified pressure-based CFD methodology - as commonly used for analysis/design of low Mach number gas turbine combustor flows - is described, which can accurately resolve acoustic wave propagation and absorption. The computational algorithm is based on the classical pressure-correction approach. This is modified to achieve (i) better capture of acoustic waves at reduced number of grid points per wavelength for low dispersion performance, and (ii) incorporation of characteristic boundary conditions to enable accurate representation of acoustic excitation (e.g. via a loudspeaker or siren), as well as acoustic reflection and transmission characteristics. The methodology is first validated against simple test cases demonstrating good numerical accuracy, then compared against classical linear acoustic analysis of acoustic and entropy waves in quasi-1D variable area duct flows. Finally, it is applied to the prediction of experimental measurements of the acoustic absorption coefficient for an orifice flow. Excellent agreement with experimental data is obtained for both linear and non-linear characteristics.

### INTRODUCTION

The recognition that an appropriate design methodology is required for detection and avoidance/management of self-sustaining combustion-induced thermo-acoustic instabilities - particularly for lean-burn combustor designs - has led to a large volume of research work in the last decade. These efforts have primarily been focussed on development of instability source modelling - identification of methods for quantitative

assessment of the flame transfer function, which describes the response of the flame to acoustic wave perturbation. This has covered both experimental and computational work ([1], [2], [3]). The resulting understanding/information has been used as input into low-order acoustic network models ([4], [5], [6]). More recently, interest has been extended beyond acoustic source description to development of an improved understanding of acoustic damping. In the industrial gas turbine field, augmentation of acoustic damping via introduction of combustion system side-branch Helmholtz resonators has received considerable attention ([7], [8]), leading to combustor designs with reduced pressure oscillations. Damping performance improvement for Helmholtz resonators by means of oscillating volumes has also been reported [9]. Further, it has been realised that strategic placement and design of passive damping devices based on perforated wall cooling flow offers a potential alternative mechanism for combined cooling/acoustic damping. Experimental studies and linear acoustic modelling approaches have been documented in [10], [11], [12].

Whilst linear acoustic modelling tools can produce very useful results, with increased geometric complexity of the combustor component(s) (cooling liner holes, resonator design etc) whose acoustic performance/responsiveness is being analysed, CFD or CAA (Computational Aero-Acoustics) modelling becomes a potentially attractive route compared to classical acoustic analysis. However, the desire to carry out combined CFD/acoustic analysis of combustors and their component parts uncovers an important computational strategy issue. Acoustic phenomena are inherently compressible in nature - this favours a density-based CFD approach. Whilst some successful CFD approaches for combustion systems are based on compressible

density-based CFD algorithms ([13], [14]), the majority of CFD methods used for low Mach number combustion prediction (particularly LES-based formulations because of the computational efficiency gained by having a CFL time step not limited by the speed of sound) are traditionally derived from a pressure-based approach ([15], [16], [17], [18]). It would be advantageous if these pressure-based CFD methods for low Mach, essentially incompressible, flows could be extended to include acoustic analysis, but this opportunity does not seem to have been fully addressed so far.

The present paper aims to close this gap by describing a modified pressure-based CFD methodology which is shown to be capable of accurately capturing acoustic wave propagation and absorption in low Mach number flows. The method is first validated by application to simple test problems such as 1D wave propagation. It is applied next to acoustic wave propagation in variable area duct flows to predict reflection and transmission coefficients for comparison with classical linear acoustic analysis [19], including also coupled entropy/acoustic wave interactions. The final demonstration of the method is to prediction of recent experimental data ([20], [21]) which have documented the flow and acoustic pressure absorption characteristics of a circular orifice in a wall with a mean pressure drop - typical of many apertures found within gas-turbine combustion systems. The unsteady velocity field and acoustic absorption coefficient are shown to be well predicted using the current methodology for a range of bias flows. The approach developed here is thus now available for use for acoustic analysis of complex geometry combustor components when incorporated into existing pressure-based CFD methods.

## NOMENCLATURE

$d_u$	velocity/pressure linkage coefficient
$d_p$	density/pressure linkage coefficient
$M$	Mach number
$p$	static pressure
$r$	acoustic reflection coefficient
$R$	gas constant
$t$	time or acoustic transmission coefficient
$T$	static temperature
$u$	velocity
$w$	characteristic variable
$W$	acoustic power
$x$	axial co-ordinate
$\Delta$	grid spacing
$\Delta t$	time step
$\lambda$	acoustic wavelength
$\gamma$	ratio of specific heats
$\rho$	density

## NUMERICAL FORMULATION

The underlying computer code used for all predictions shown here is based on the classical pressure-correction approach

commonly used for combustor modelling (typically a variant of the SIMPLE pressure-correction method [22]). This has been modified to include:

- (i) Higher convection discretisation accuracy – to achieve a reduced number of points per acoustic wavelength for low numerical dispersion and diffusion,
- (ii) Pressure-density coupling - to include compressibility effects in particular for acoustic phenomena in low Mach number shock free flows – here labelled as ‘mildly’ compressible flows,
- (iii) Characteristic boundary conditions - for correct wave propagation and inlet/outlet boundary condition specification.

The algorithm modifications selected in each of these areas are outlined next. For simplicity this is done using 1D illustrations, although the modifications have been introduced into a fully 3D CFD code.

### Higher order discretisation

In order to predict accurately wave propagation through space and time it is required that the numerical scheme should preserve the wave shape and frequency during propagation (low numerical diffusion and dispersion). Typical 2<sup>nd</sup> order accurate CFD convection discretisation methods, quite adequate for both RANS and LES CFD dominated by turbulent mixing processes, require large number of grid points per acoustic wavelength (40-50) to reduce damping and dispersion errors to acceptable levels. This has led to development of specialised Computational Aero-Acoustics (CAA) methods. One of the best-known CAA methods is Tam and Webb’s DRP (Dispersion Relation Preserving) scheme [23], where the discretisation is optimised for minimum dispersion, although some numerical dissipation has to be built in to provide stability; a similar approach with even higher (up to 10<sup>th</sup>) order accuracy has been suggested by Bogey and Bailly [24]. An alternative approach, motivated by a similar need to capture sharp gradients and avoid numerical oscillations in strongly compressible flows containing shocks is the WENO (Weighted Essentially Non-Oscillatory) scheme described by Shu and co-workers ([25], [26]). To compare these schemes with standard incompressible RANS/LES CFD methods such as Upwind Differencing (UD), Central Differencing (CD), and Total Variation Diminishing (TVD) schemes, test problems which highlight low damping and dispersion performance were selected.

The first test case is a 1D unsteady pure convection problem for a scalar property whose profile is pre-specified (a Gaussian shape in space:  $0.5\exp[-\ln\{2(x-x_0/\sigma)^2\}]$ , where  $x_0$  indicates the location of the maximum and  $\sigma$  is the standard deviation), which propagates at constant speed with unchanged shape. This problem was proposed at a workshop on CAA methods [27]. Various wave profile shapes were proposed in this linear propagation problem, depending on the ratio of the profile width to grid size (represented by  $\sigma/\Delta$ ). For long waves ( $\sigma/\Delta = 15$ ) all 2<sup>nd</sup> order or higher schemes (CD, TVD, DRP and

WENO) capture the waveform well with barely noticeable dispersion or dissipation errors. For shorter waves ( $\sigma/\Delta = 6$ ) scheme performance starts to differ. This is illustrated in Fig. 1, where WENO is seen to out-perform the other schemes, with no dispersion, little numerical diffusion and smaller phase error.

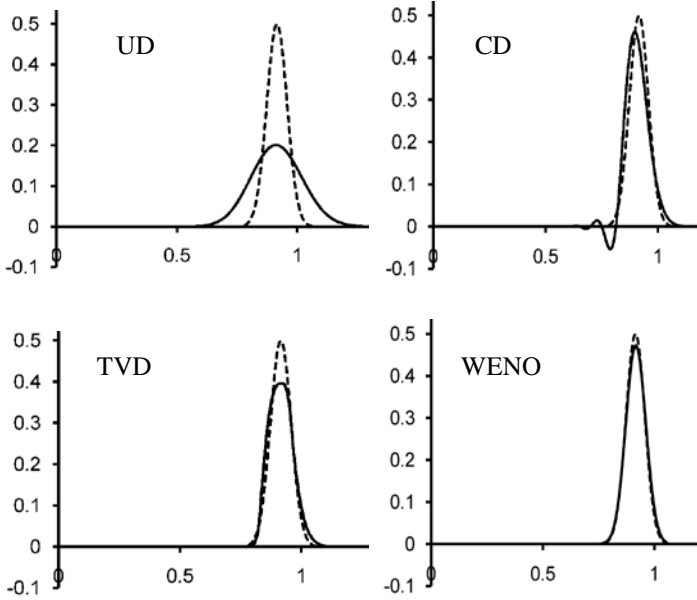


Figure 1: 1D scalar propagation test case; comparison between exact (dashed line) and CFD (solid line) solutions for  $\sigma/\Delta = 6$

The second test case is a 2D pure convection problem (zero physical diffusion) previously studied by Dianat et al [28]. The problem consists of a sharp profile in a scalar property being convected in a specified velocity field around a semi-circle in a 2D plane. Since errors (numerical diffusion in particular) are worsened when the velocity is at an angle to cell faces, this is a good test case to reveal artificial damping and numerical spreading of wave shape. Fig. 2 indicates the WENO solution for this problem on a mesh of 80 x 40 cells. The predicted scalar contours show little evidence of numerical spreading, but oscillations as a result of small dispersion errors can be seen. The global error evaluated by comparison with the exact solution is shown in Fig. 3, comparing different numerical schemes and different mesh sizes. 1<sup>st</sup> order UD clearly leads to large errors. The 2<sup>nd</sup> order CD and TVD schemes perform better, with errors an order of magnitude smaller on a given grid, and also a steeper gradient for error reduction. TVD shows smaller errors because it reduces the high dispersion errors of CD. The DRP schemes of [23] and [24] perform no better than the WENO scheme of [26], except on the finest meshes (which will not always be affordable in practical CFD calculations). This is because, although the DRP schemes formally have a 6<sup>th</sup> or even higher order of accuracy, the added dissipation to produce acceptable stability interferes with this. Only for the finest mesh does a DRP 8<sup>th</sup> order scheme show any benefit, and then only marginally. In general the WENO scheme is better on coarse meshes than the DRP schemes, hence the WENO

scheme was considered to perform better in this test case in terms of accuracy and robustness over a range of mesh sizes.

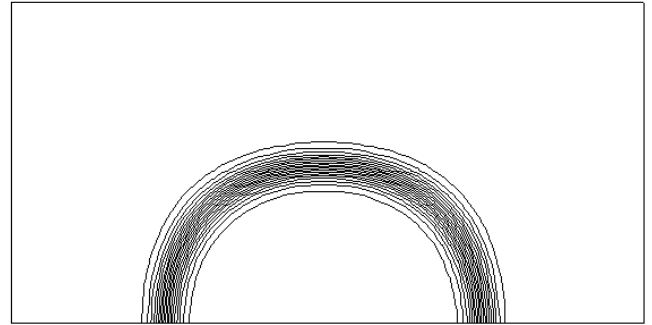


Figure 2: 2D scalar convection test case (WENO solution)

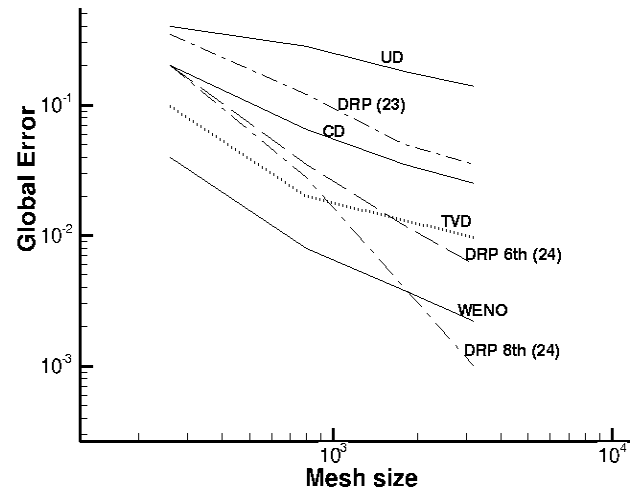


Figure 3: 2D scalar convection test case; error vs mesh size for various schemes

As a final assessment of performance for low acoustic dissipation and dispersion errors, the test case selected by Foeller and Polifke [29] has been selected. This corresponds to an acoustic sine wave of amplitude 0.2m/s at 100Hz propagating in 1D along a duct whose length is adjusted to fit 10 acoustic wavelengths. The mean flow in the duct is 0.25m/s

$\Delta/\lambda$	Dissipation error (%)			Dispersion error(%)		
	Ref [29]	TVD	WENO	Ref [29]	TVD	WENO
10	34.7	23.2	14.7	2.89	0.02	0.04
20	2.8	5.4	1.7	0.08	0.02	0.03
30	1.2	1.5	0.6	0.05	0.02	0.02
40	0.4	0.6	0.2	0.05	0.02	0.02

Table 1 Linear acoustic wave propagation; scheme comparison at various cells/acoustic wavelength.

Simulations were carried out with various ratios of cell size to acoustic wavelength ( $\Delta/\lambda$ ). Sinusoidal forcing was applied at the inlet boundary using the characteristic scheme described below. Predicted downstream time series and spatial information after 10 acoustic wavelengths were post-processed to evaluate acoustic dissipation (from predicted wave amplitude) and dispersion (from predicted wavelength) relative to the exact values. These dissipation and dispersion errors are shown in Table 1. Comparison between the current 2<sup>nd</sup> order TVD and 5<sup>th</sup> order WENO schemes as well as the 2<sup>nd</sup> order Lax-Wendroff scheme used in [29] are shown. In general the WENO scheme produces dissipation errors half those of 2<sup>nd</sup> order schemes at the same resolution. Dispersion errors for all schemes are very small except for the most under-resolved mesh for the 2<sup>nd</sup> order Lax-Wendroff method. Based on this range of test cases, the WENO scheme was selected as providing best overall performance.

#### Pressure – Density Coupling

Traditional density-based compressible CFD algorithms become stiff at low Mach number [30] when the density becomes a weak function of pressure; pre-conditioning techniques [31] have been suggested to solve this problem, but in general the computational efficiency in comparison to pressure-based methods for low Mach number flows is still deficient. A review of the evolution of pressure-based methods over the last 40 years has been provided in [22]. Modifications for compressible flow were first suggested around 1990 [32], [33]. McGuirk and Page [32] showed that for accurate shock capturing on a given mesh, the compressible modification is best conducted by first changing the solution variables from velocities (as normally used in pressure-based methods) to momentum components (as normally used in density-based methods) before deriving the modified pressure-correction equation. Since we are here only interested in compressibility due to acoustic perturbations, with essentially incompressible mean flow (‘mildly’ compressible flow), this alternative is not required, and we may follow the methodology as suggested by Karki and Patankar [33], which retains velocity as the primary variable and adopts a linearisation process to derive the compressible pressure-correction equation, as described below.

A compressible pressure-correction equation must include a pressure/density linkage. How this is introduced, following [33] and [34] is illustrated here in 1D using Cartesian coordinates; this is generalised in the usual way to 3D in the CFD solver used as described below. The pressure-correction equation is derived from the continuity equation, which in 1D may be written:

$$\frac{\partial \rho}{\partial t} + \frac{\partial \rho u}{\partial x} = 0$$

The mass flux term in this equation must be linearised, since both density and velocity are influenced by the local static pressure field. The pressure-correction technique is an implicit method, so we first decompose the solution at the new time level into a guessed (starred) value and a correction:

$$\rho^{n+1} = \rho^* + \rho' \quad u^{n+1} = u^* + u'$$

The guessed value of the density field is evaluated from the gas law using the old time level of pressure ( $p^*$ ) and the guessed velocity field is evaluated from solution of the discretised momentum equations with pressure gradients calculated also using  $p^*$ . Substituting into the continuity equation leads to:

$$\frac{\rho'}{\Delta t} + \frac{\partial}{\partial x} [(\rho^* + \rho')(u^* + u')] = 0$$

The mass flux term is linearised by ignoring 2<sup>nd</sup> order products and the continuity equation thus becomes:

$$\frac{\rho'}{\Delta t} + \frac{\partial}{\partial x} [\rho^* u' + \rho' u^*] = 0$$

From the discretised form of the momentum equation, a relation between velocity-correction and pressure-correction gradient may be extracted (see [33], [34]):

$$u' = -d_u \frac{\partial p'}{\partial x}$$

where  $d_u$  represents a coefficient which depends on the precise discretisation adopted. Similarly, a relation between density-correction and pressure-correction may be chosen:

$$\rho' = d_\rho p' \quad d_\rho = \frac{\partial \rho}{\partial p} = \frac{1}{\gamma RT}$$

$d_\rho$  may be evaluated in various ways, from an equation of state, or, as above, assuming an isentropic process; this does not affect the final result, but only the approach to convergence. Substituting these correction relations into the continuity equation produces the final pressure-correction equation:

$$\frac{p'}{\gamma RT \Delta t} + \frac{\partial}{\partial x} \left[ -\rho^* d_u \frac{\partial p'}{\partial x} \right] + \frac{\partial}{\partial x} \left[ \frac{u^*}{\gamma RT} p' \right] = -\frac{\partial \rho^* u^*}{\partial x}$$

The second term on the left hand side contains a diffusion-like term and the third term is convection-like. The ratio of the two terms is proportional to the inverse square of Mach number. At low Mach numbers, the diffusion term is dominant and the pressure-correction equation behaves as in an incompressible flow (an elliptic equation). As Mach number increases, the convection term becomes more dominant and the equation behaves like a hyperbolic equation. In this way the pressure-

correction equation changes type as local conditions represent either essentially incompressible or compressible flow.

### Characteristic Boundary Conditions

In solving acoustic problems, it is essential to use appropriate boundary conditions at flow inlets/outlets to provide correct input of acoustic excitation waves, and to prevent spurious, non-physical wave reflections at these solution domain boundaries. Many researchers have studied this issue; comprehensive reviews can be found in Poinso and Veynante [6], Hirsch [35], Colonius [36], Thompson [37], and Hedstrom [38]. In the current work, where we are mainly interested in ensuring accurate characterisation of input acoustic excitation due to sirens or loudspeakers, and accurate estimation of the amplitude of acoustic waves leaving the solution domain, a simple 1D approach to implementation of characteristic boundary conditions for subsonic inlets and outlets within a pressure-based formulation forms an optimum starting point. If necessary, the same approach could be easily modified to incorporate more complex characteristic treatments (e.g. [6]).

### Subsonic Inlet

Hirsch [35] has derived the 1D equations governing the propagation of acoustic perturbations in primitive variables (u, p) under isentropic conditions for right and left travelling waves. These may be written as follows:

$$\frac{\partial u'}{\partial t} + \frac{1}{\rho_m c_m} \frac{\partial p'}{\partial t} + (u_m + c_m) \left( \frac{\partial u'}{\partial x} + \frac{1}{\rho_m c_m} \frac{\partial p'}{\partial x} \right) = 0$$

$$\frac{\partial u'}{\partial t} - \frac{1}{\rho_m c_m} \frac{\partial p'}{\partial t} + (u_m - c_m) \left( \frac{\partial u'}{\partial x} - \frac{1}{\rho_m c_m} \frac{\partial p'}{\partial x} \right) = 0$$

where a dash superscript indicates an acoustic property and a subscripted variable indicates a mean flow property. These equations are discretised using a 1<sup>st</sup> order Euler method in time and upwind differencing in space. In the following additional subscripts indicate the particular nodal point in question - 'i' is the boundary node, 'in' is the first interior node and  $\infty$  represents the (assumed known) conditions far upstream of the inlet; a superscript indicates the temporal index. The third part of the above equations are discretised as:

$$w_{right}^n = (u_{m,i}^n + c_{m,i}^n) \left[ \frac{(u_i'^n - u_\infty'^n)}{\Delta x} + \frac{1}{\rho_{m,i}^n c_{m,i}^n} \frac{(p_i'^n - p_\infty'^n)}{\Delta x} \right]$$

$$w_{left}^n = (u_{m,i}^n - c_{m,i}^n) \left[ \frac{(u_i'^n - u_\infty'^n)}{\Delta x} - \frac{1}{\rho_{m,i}^n c_{m,i}^n} \frac{(p_i'^n - p_\infty'^n)}{\Delta x} \right]$$

Leading to:

$$\frac{u_i'^{n+1} - u_i'^n}{\Delta t} + \frac{1}{\rho_{m,i}^n c_{m,i}^n} \left( \frac{p_i'^{n+1} - p_i'^n}{\Delta t} \right) = -w_{right}^n$$

$$\frac{u_i'^{n+1} - u_i'^n}{\Delta t} - \frac{1}{\rho_{m,i}^n c_{m,i}^n} \left( \frac{p_i'^{n+1} - p_i'^n}{\Delta t} \right) = -w_{left}^n$$

By adding and subtracting, the boundary conditions for acoustic velocity and pressure perturbations are obtained:

$$u_i'^{n+1} = u_i'^n - \frac{\Delta t}{2} (w_{right}^n + w_{left}^n)$$

$$p_i'^{n+1} = p_i'^n - \frac{\Delta t \rho_{m,i}^n c_{m,i}^n}{2} (w_{right}^n - w_{left}^n)$$

All remaining variables (e.g.  $\rho$ ) are obtained using isentropic relations and the equation of state.

### Subsonic Outflow

In this case, conditions at infinity far-downstream of the outlet are assumed known and the boundary conditions can be obtained using the same relations as for a subsonic inlet bc, by interchanging u, p variable locations, i.e.:

$$u_{in}'^n \rightarrow u_\infty'^n, p_{in}'^n \rightarrow p_\infty'^n \text{ and } u_\infty'^n \rightarrow u_{in}'^n, p_\infty'^n \rightarrow p_{in}'^n$$

## COMPUTATIONAL IMPLEMENTATION

A 3D pressure-based CFD solver previously applied to the solution of incompressible flows relevant to combustor components ([39], [40]) has been modified as described in the previous section to allow simulation of acoustic phenomena in low Mach number flow. The basic code follows the cell-centred, finite-volume, implicit discretisation methodology described in Ferziger and Peric [41]. To deal with complex geometries the CFD solver uses a body-fitted curvilinear non-orthogonal grid within a multi-block structured mesh approach, as well collocated solution variable storage. In the RANS form of the equations used here, the eddy viscosity was obtained using a standard high Re k- $\epsilon$  turbulence model, with Durbin's [42] realisable correction to avoid the stagnation point anomaly; wall functions were used at all wall boundaries. It is important to point out that a detailed study of the adequacy of the turbulence model for acoustic damping problems was not the intention here. Rather the model was selected for two principle reasons: (i) the k- $\epsilon$  model was originally calibrated to produce realistic levels of turbulent viscosity in free shear layers such as are present in the jets emerging from the orifice problem studied below, so no excess damping of acoustics was expected, (ii) the Durbin [42] correction is known to improve the model performance in rapidly accelerating flows such as

found on entry to the orifice. Further study of the optimum RANS turbulence closure to be adopted in acoustic damping flow problems would be clearly beneficial. Finally, pressure-velocity decoupling associated with collocated storage was avoided using Rhie and Chow [43] pressure smoothing.

## RESULTS

### Method Validation – prediction of acoustic and entropy waves

As a first step in validating the pressure-based methodology proposed here, the modified CFD code was applied to the problem of transmission, reflection and interaction of acoustic and entropy waves in subsonic quasi-1D, variable area ducts. This problem has previously been studied by Barton [19] using a numerical solution of the classical linear acoustic approach to analysis of quasi-1D duct flows; these solutions are available to compare with current CFD predictions. The 1<sup>st</sup> test case shown here is the prediction of acoustic transmission and reflection coefficients for a diffuser for various inlet Mach numbers/input wave frequencies. Four wave components must be considered in specifying boundary conditions and determine the acoustic input/output relationships these are:

- Wave 1 - downstream propagating acoustic wave at duct inlet
- Wave 2 - upstream propagating acoustic wave at duct inlet
- Wave 3 - downstream propagating acoustic wave at duct outlet
- Wave 4 - upstream propagating acoustic wave at duct outlet.

When a pure downstream propagating acoustic wave is input at diffuser inlet, part of this wave will be continue to be transmitted downstream but part will be reflected because of the changing duct area. Appropriate reflection and transmission coefficients may be defined (see [19]), for example:

- $t_{dd}$  – transmission coefficient – ratio of downstream propagating wave at outlet to downstream propagating wave at inlet,
- $r_{ud}$  – reflection coefficient – ratio of upstream propagating wave at inlet to downstream propagating wave at inlet,
- $t_{uu}$  – transmission coefficient – ratio of upstream propagating wave at inlet to upstream propagating wave at outlet,
- $r_{du}$  – reflection coefficient – ratio of downstream propagating wave at outlet to upstream propagating wave at outlet,

Fig. 5 shows the wave components for a 1:4 area ratio 1m long diffuser as used in [19]. All acoustic coefficients were calculated in two CFD runs where either: (i) wave 1 was specified to be finite (e.g. a loudspeaker input) and wave 4 was specified to be zero (no incoming wave at diffuser outlet), or (ii) wave 1 was set to zero and wave 4 was set at a finite value. The CFD predictions are compared with the solution from [19] in Fig. 6 for an excitation frequency of 1000 rad/s in terms of reflection and transmission coefficients (similar results were obtained for 100 rad/s). In Fig.6 the symbols represent data from [19] and the lines CFD predictions. It is clear that in general in such a flow, acoustic transmission in the flow

direction is low (less than 1, and increasing with M), as is reflection of upstream propagating waves at diffuser outlet (less than 1 but decreasing slightly with M). On the other hand, transmitted downstream propagating inlet waves experience an increase in amplitude, as do upstream propagating waves from diffuser outlet. Excellent agreement is obtained over the whole range of Mach numbers.

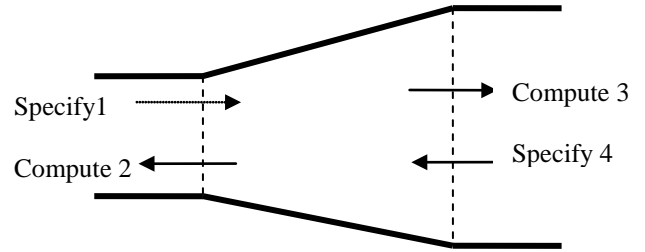


Figure 5 : Schematic of diffuser with acoustic wave boundary conditions

Following a similar procedure it is possible to define a 2<sup>nd</sup> test problem for a convected entropy wave (hot spot) which excites an acoustic response when passing through a variable area duct. Fig 7 defines the wave components relevant to this problem. A specified amplitude/frequency entropy wave was input at inlet, this time for a 4:1 area ratio 1m long nozzle (to simulate a combustor exit transition nozzle), with a zero amplitude acoustic wave specified as propagating downstream at inlet. The relevant transmission/reflection coefficients here are:

- $t_{de}$  – transmission coefficient – ratio of downstream propagating acoustic wave at outlet to convected entropy wave at inlet,
- $r_{ue}$  – reflection coefficient – ratio of upstream propagating acoustic wave at inlet convected entropy wave at inlet.

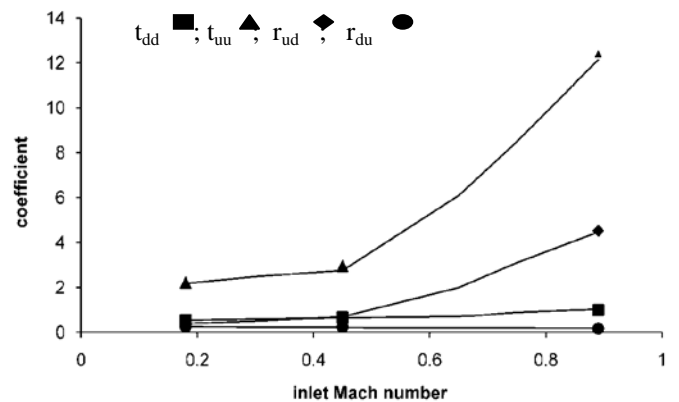


Figure 6 : Acoustic wave transmission and reflection coefficients for input wave frequency = 1000 rad/s  
Lines-CFD predictions, symbols [19]

Fig. 8 shows again excellent agreement of CFD predictions with the linear acoustic analysis from [19] for various nozzle

inlet Mach numbers. The solutions show how a propagating entropy wave can excite a significant acoustic response – a factor of 10-20 amplification in terms of  $\text{Pa}^0/\text{K}$ . This problem is an important test case; the phenomenon of ‘entropy noise’ as examined in this test problem is attracting increasing attention in the gas turbine combustor community [44].

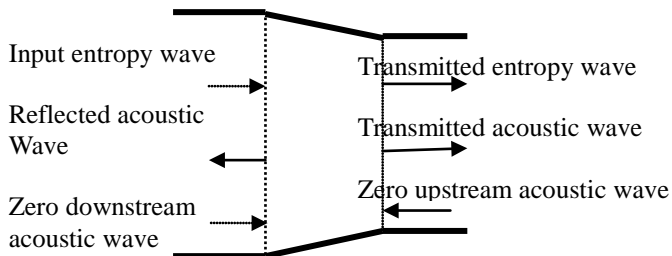


Figure 7: Nozzle with acoustic/entropy wave conditions

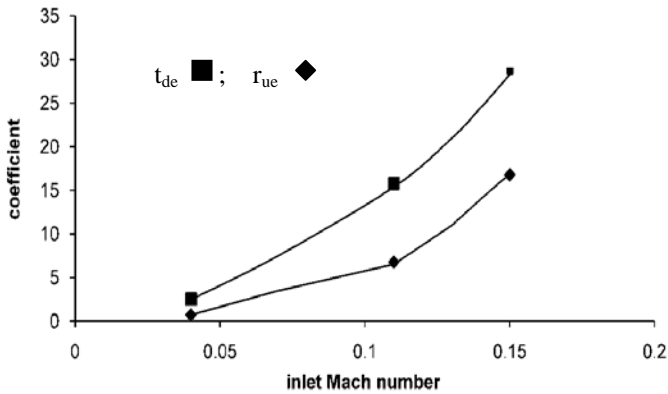


Figure 8 : Entropy wave transmission and reflection coefficients for input wave frequency = 100 rad/s Lines-CFD predictions, symbols [19]

*Method Application – prediction of acoustic power absorption*

To illustrate the application of the developed methodology to the problem of prediction of acoustic absorption/damping due to orifice flows - of significant current interest in terms of possible passive damping opportunities using porous wall cooling flow designs - predictions of the experimental work of Rupp et al [20], [21] have been undertaken. The flow configuration used in these measurements is shown in Fig. 9. A single round orifice with a diameter of 12.7mm and a thickness of 6mm was placed in a rectangular duct of cross-section 120mm x 120mm. The orifice was subjected to acoustic wave excitation using a downstream loudspeaker. To represent the loudspeaker in the CFD solution, an upstream propagating acoustic wave was specified at the downstream end of the solution domain (wave component 4 in Fig. 5). As in the experiment a frequency of 125 Hz with an amplitude from 115dB – 143dB was applied. Upstream of the orifice, the duct length was fixed at 687mm; a mean flow enters the solution

domain, specified via the measured pressure drop across the orifice. The length of the upstream duct was chosen to correspond to a quarter wavelength and acoustically closed boundary conditions were imposed at duct inlet ( $w_{right} = -w_{left}$ ) to ensure a pressure node (zero pressure fluctuation) would be formed at the upstream plane of the orifice, as was arranged in the measurements. A block-structured grid was generated using ICEM-CFD, avoiding the centreline singularity by including an H-grid block at the centre of the domain. Fig. 10 shows the grid in the duct cross section as well as at the orifice plane.

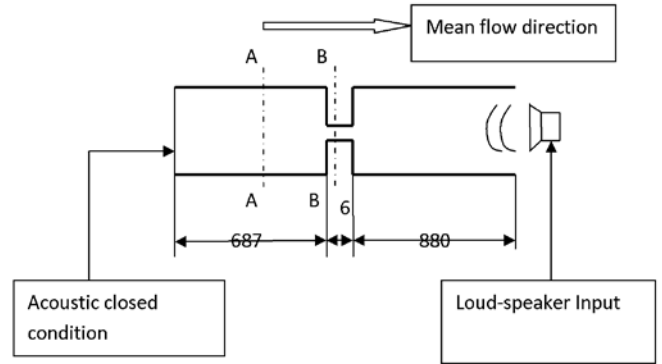


Figure 9: Schematic of orifice and duct/excitation configuration (dimensions in mm)

Two mean flow conditions - zero mean flow and 500 Pa pressure drop across the orifice - were chosen for the current study. The acoustic absorption coefficient was calculated as in the experiments using the difference between acoustic power propagating towards and away from the orifice. The incident

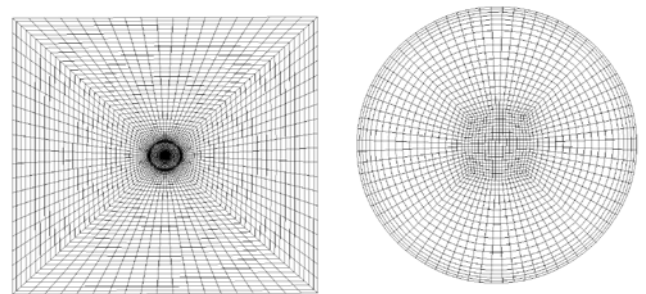


Figure 10: Mesh at duct section A-A and orifice section B-B.

upstream propagating acoustic wave from the loudspeaker ( $p_{di}^-$ ), which was input via the downstream characteristic boundary condition is partly transmitted to the upstream duct ( $p_{ur}^+$ ) and also partly reflected ( $p_{dr}^+$ ) to propagate downstream. Because of the use of an acoustically closed boundary condition at upstream duct inlet, the transmitted wave will be fully reflected ( $p_{ur}^+$ ).

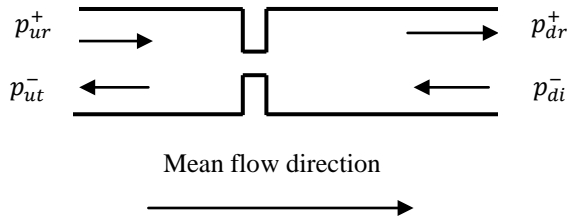


Figure 11: Wave decomposition in the duct.

The acoustic power of upstream and downstream propagating waves and the absorption coefficient ( $A$ ) are calculated from :

$$W^- = \left( \frac{\text{area of duct}}{2\rho_m c_m} \right) \left( |p^-|^2 \right) (1-M)^2$$

$$W^+ = \left( \frac{\text{area of duct}}{2\rho_m c_m} \right) \left( |p^+|^2 \right) (1+M)^2$$

$$A = \frac{W_{di}^- + W_{ur}^+ - W_{dr}^+ - W_{ut}^-}{W_{di}^- + W_{ur}^+}$$

For 500 Pa mean pressure drop across the orifice the mean flow was first established without inputting any acoustic perturbation with turbulence modelled using Durbin's [43] realisable constraint in the  $k-\epsilon$  model to avoid anomalies due to the high acceleration upstream of the orifice. WENO was used for the convective terms and the transient term was discretised using a 2<sup>nd</sup> order implicit method. Once the mean flow was established, wave contributions corresponding to the acoustic excitation were then applied.

Figure 12 shows comparison between the absorption coefficient predicted using the CFD method developed here with the experimental data of Rupp et al [20]. Good agreement can be seen for all excitation pressure amplitudes as well as for both mean flow conditions. At 500 Pa pressure drop, the absorption displays a constant value until an excitation pressure level of ~140dB. This indicates a linear acoustic phenomenon. Further increase in pressure amplitude begins to show non-linear effects as the absorption coefficient starts to increase slightly. It should be noted that this behaviour is observed to occur at the same excitation level in the CFD predictions as in the test data. Rupp et al [20] commented that this onset of non-linearity is associated with the excitation amplitude increasing to a level where the unsteady pressure effect at the downstream orifice face is able to reverse the flow through the orifice overcoming the effect of the mean  $\Delta p$ . The images of the CFD predicted flow structure at various stages of the acoustic cycle shown in Fig. 13 confirm this description. Fig 13 shows predicted axial velocity contours and streamline patterns for 5 points in the acoustic cycle, starting at a time when the acoustic pressure perturbation at the downstream orifice face is zero and about to start increasing. For the 5 flowfield snapshots shown, the first is

at the initial time and the other 4 are separated by a phase of  $\pi/2$  from the initial time. For 137dB excitation, the jet through the orifice increases and decreases in strength and width as the acoustic perturbation changes, but the flow is always forwards through the orifice, and the flow external to the jet corresponds

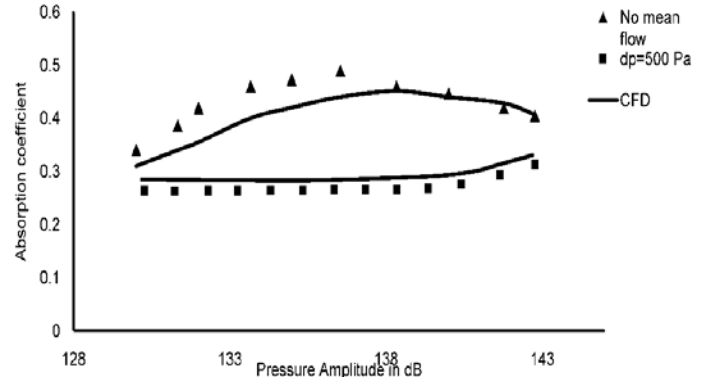


Figure 12: Absorption coefficient with and without mean flow, symbols – Rupp et al [20], lines – CFD predictions.

to a pure entrainment process. Note that the streamline pattern in the region outside the jet which visualises the entrainment into the jet shear layers is not quite symmetrical. This is a URANS prediction carried out assuming no symmetry planes, so the jet is free to 'wander' off centreline, and does so. For increased excitation to 143 dB, the jet flow through the orifice experiences a stronger deceleration, eventually leading to a small separation region inside the orifice. This is seen best at the second time instant, where streamlines within the orifice move away from the walls and a close-up indicates negative velocities - see Fig 14 which shows flow features inside the orifice at the second time instant; no internal recirculation at 137dB but a clearly formed eddy at 143dB. This creates a 'starting vortex' as the jet begins to flow forward again (seen forming in the third frame). The growth in size and downstream propagation of the starting vortex ring is clearly visible in Fig 13 for 143dB excitation, but not present at all at the 137dB level. The kinetic energy of this vortex is responsible for the increase in acoustic damping coefficient, since the vortex kinetic energy (subsequently dissipated into internal energy) is extracted from the acoustic energy.

The non-linear behaviour can of course be seen most clearly, and for all excitation amplitudes in the zero mean flow data/predictions shown in Fig. 12 and in the flow structure images in Fig. 15. Vortex rings are predicted to exist at all pressure levels and the strength of the vortex increases, leading to enhanced acoustic absorption, as the pressure level increases. However, a peak in the acoustic absorption curve is observed in the experiments at ~137dB, and in the CFD predictions at 139dB. The decrease is due (see [20] and [45]) to the fact that above a certain level of excitation, a maximum circulation in the vortex ring is reached; further increase in acoustic pressure amplitude leads more to a strengthening of the secondary jet

[45], which is formed in the vortex central region and trails behind it, rather than increased vortex strength; this is less effective so damping coefficient falls. Fig. 15 shows a stronger secondary jet for excitation above 139dB.

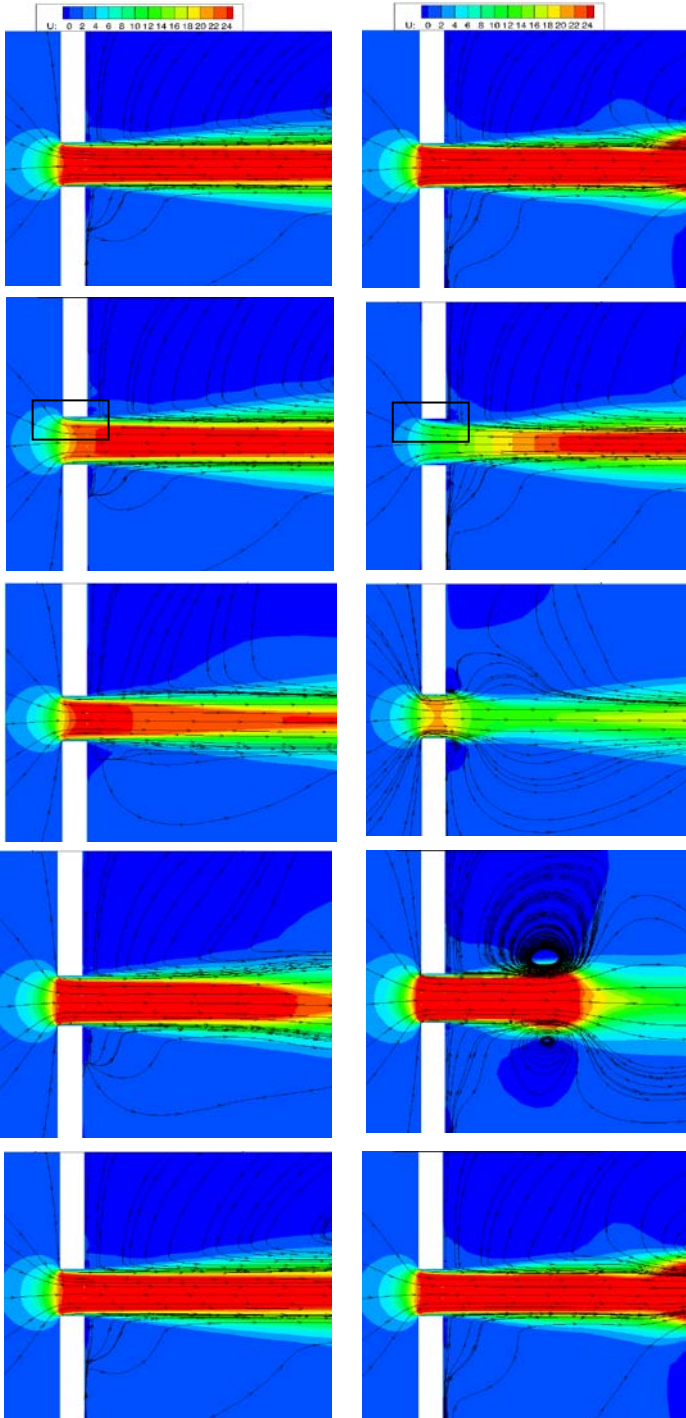


Figure 13: Flow structure for linear (left – 137dB) and nonlinear (right - 143dB) excitation; bias flow at 500 Pa  $\Delta p$ . (Boxed regions at 2<sup>nd</sup> time level – see Fig.14 below)  
It should be noted that the high Re turbulence model used here

is almost certainly responsible for the underpredicted absorption coefficient for zero mean flow, particularly at low excitation levels. Whereas for the case with mean flow the Reynolds numbers of the jet from the orifice and in the duct flow was  $\sim 50,000$ , for zero mean flow it was an order of magnitude smaller, so low Re effects not captured by the current turbulence model can be expected. A zero mean flow calculation with no turbulence model improved the predicted

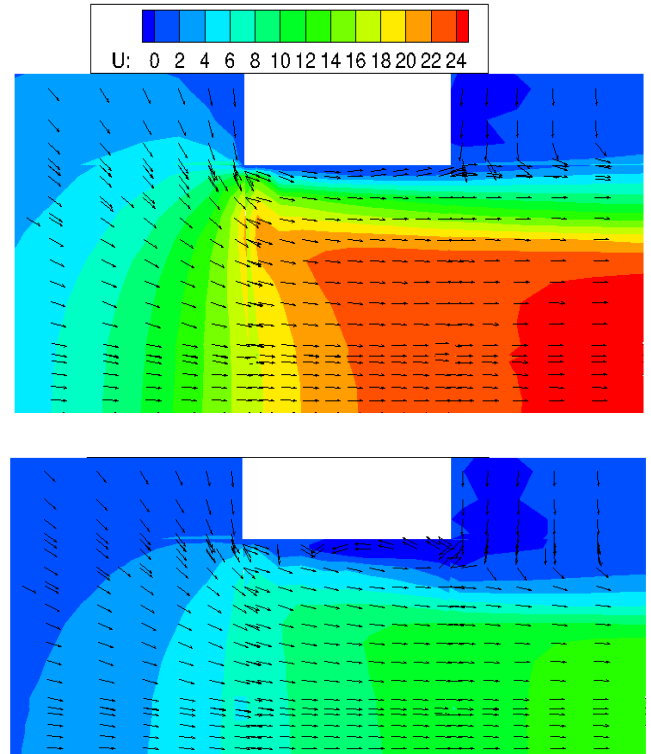


Figure 14: Predicted velocity vectors inside orifice for 500Pa mean bias  $\Delta p$  at second time instant of Fig 13; 137dB (top) and 143dB (bottom).

absorption coefficient at 133dB from 0.38 (with turbulence model) to 0.41 (without model), compared to the measured value of 0.46. Clearly a careful study of the optimum (probably low Re) turbulence closure would be valuable for acoustic damping type flows such as considered here.

## SUMMARY AND CONCLUSIONS

A mildly compressible pressure-based CFD methodology is described for prediction of acoustic phenomena in low Mach No. flows relevant to gas-turbine combustors and their components. Modifications to a conventional pressure-correction method were implemented and tested. The developed solver was validated against linear acoustics analysis for acoustic & entropy input-output relations for variable area ducts. The capability of the method was indicated by successful comparison against experimental data for acoustic absorption in flow through an orifice. On the basis of the work presented here

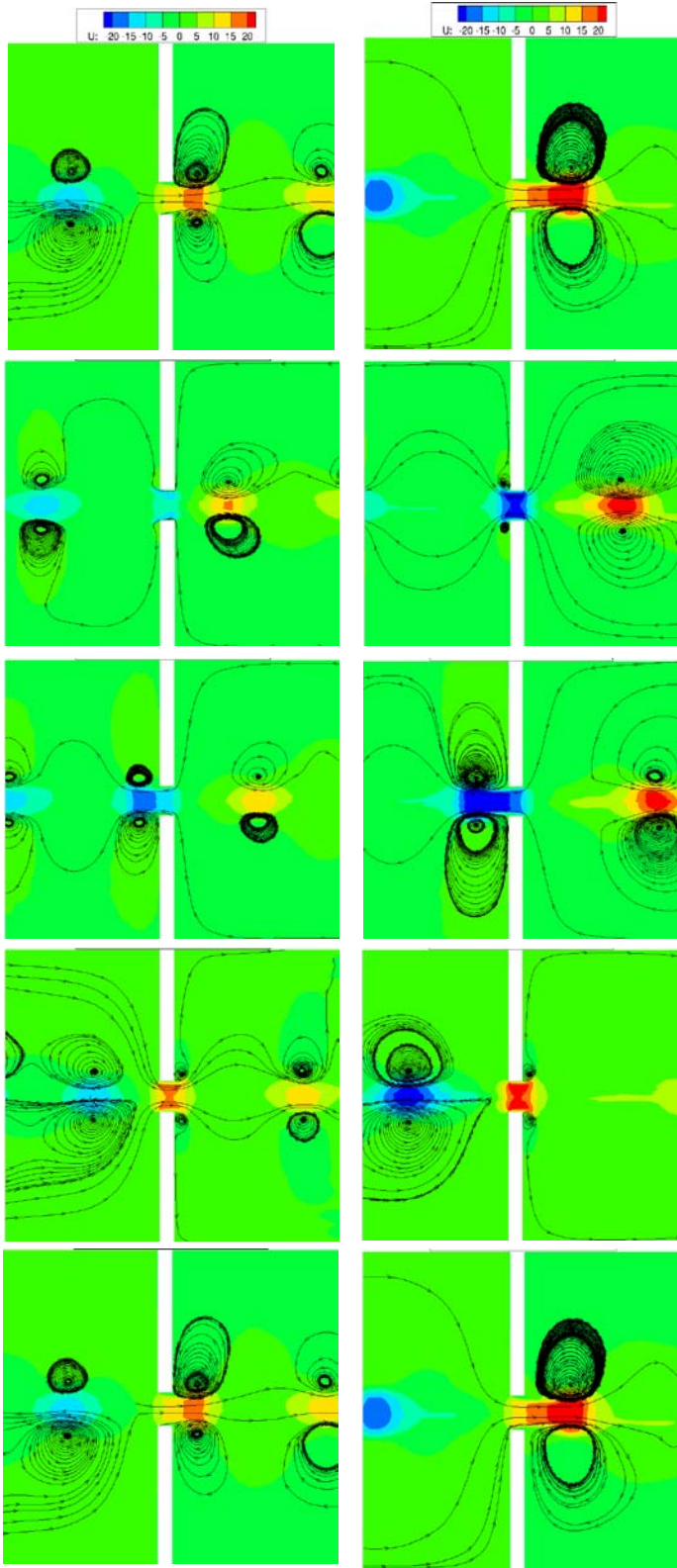


Figure 15: Flow structure at 136dB (left) and 143dB (right) excitation; zero mean flow

the methodology shows considerable promise for incorporation into other pressure-based CFD codes and for use in acoustic performance assessment relevant to combustors, such as passive damper designs. To establish complete confidence in the approach, it would also be useful to test it against higher frequency applications, using test data as presented for example in Testud et al [46].

## ACKNOWLEDGMENTS

This work was carried out in the Loughborough University Technology Centre in Combustion Aerodynamics; the authors acknowledge financial support from UK DTI (ANTLE) as well as discussions with colleagues at Rolls-Royce (Derby).

## REFERENCES

1. Schuller, T., Ducruix, S., Durox, D., Candel, S., "Modelling tools for the prediction of premixed flame transfer functions", *Proc. of the Combustion Institute*, **29**, pp107-113, 2002.
2. Kim, D, Lee, J. G., Quay, B. D., Santavicca, D. A., Kim, K., Srinivasan, S., "Effect of flame structure on the flame transfer function in a premix gas turbine combustor", *ASME Jnl. of Eng. For Gas Turbines and Power*, **132**, pp 021502-1 -7, 2010.
3. Chong, L.T. W., Komarek, T., Kaess, R., Foeller, S., Polifke, W., "Identification of flame transfer functions from LES of a premixed burner", ASME GT2010-2276, ASME Turbo Expo 2010, Glasgow, UK, June, 2010.
4. Dowling, A. P. and Stow, S. R., "Acoustic analysis of gas turbine combustors", *AIAA Jnl. of Propulsion and Power*, **19**, pp 751-764. 2003.
5. Sattelmayer, T. and Polifke, W., "Assessment of methods for the computation of the linear stability of combustors", *Combust. Science & Tech.*, **175**, pp 453-476, 2003.
6. Poinso, T., Veynante, D., "Theoretical and numerical combustion", 2<sup>nd</sup> Edition, Edwards, Phil., USA, 2005.
7. Gysling, D. L., Copeland, G. S., McCormick, D. C., Proscia, W., "Combustion system damping augmentation with Helmholtz resonators", *ASME Jnl. of Eng. for Gas Turbines & Power*, **122**, pp 269-274, 2000.
8. Dupere, I. D. J. and Dowling, A. P., "The use of Helmholtz resonators in a practical combustor", *ASME Jnl. of Eng. For Gas Turbines and Power*, **127**, pp 268-275, 2005.
9. Zhao, D., A' Barrow, C., Morgans, A. S., Carrotte, J., "Acoustic damping of a Helmholtz resonator with an oscillating volume", *AIAA Jnl.*, **47**, pp 1672-1679, 2009.
10. Rehman, S. F. and Eldredge, J. D., "Numerical investigation of a bias-flow perforated liner for damping of thermoacoustic instabilities", ASME GT2007-27319, 2007.
11. Camporeale, S. M., Fortunato, B., Mastrovito, M., "Prediction of thermoacoustic instability in combustion chambers equipped with passive dampers", ASME GT2008-51387, 2008.
12. Bhayaraju, Y., Schmidt, J., Kashinath, K., Hochgreb, S., "Effect of cooling liner on acoustic energy absorption and flame response", ASME GT2010-22616, 2010.

13. Selle, L., Lartigue, G., Poinso, T., Koch, R., Schildmacher, K-U., Krebs, W., Prade, B., Kaufmann, P., and Veynante, D., "Compressible Large Eddy Simulation of turbulent combustion in complex geometry on unstructured meshes", *Combustion and Flame*, 137, pp 489-505, 2004.
14. Menon, S. and Patel, N., "Sub-Grid modelling for simulation of spray combustion in large-scale combustors", *AIAA Jnl.*, 44, pp 709-723, 2006.
15. Anand, M. S., Zhu, J., Connor, C. and Razdan, M. K., "Combustor flow analysis using an advanced finite-volume design system", ASME 99-GT-273, 1999.
16. Malecki, R. E., Rhie, C. M., McKinney, R. G., Ouyang, H., Syed, S. A., Colket, M. B. and Madabushi, R. V., "Application of an advanced CFD-based analysis system to the PW6000 Combustor to optimise exit temperature distribution – Part I: Description and validation of the analysis tool, ASME 2001-GT-62, 2001.
17. Snyder, T. S., Stewart, J. F., Stoner, M. D. and McKinney, R. G., "Application of an advanced CFD-based analysis system to the PW6000 Combustor to optimise exit temperature distribution : comparison of predictions to full-annular rig test data", ASME 2001GT64, 2001.
18. James, S., Anand, M. S., Sekar, B., "Towards improved prediction of aero-engine combustor performance using Large Eddy Simulations", ASME GT2008-50199, 2008.
19. Barton, J.P, "Acoustic and entropy wave input-output relationships for quasi-1D gas flows", *Jnl. of the Acoustical Soc. of America*, 80, pp 340-346, 1989.
20. Rupp, J., Carrotte, J.F., Spencer, A., "Interaction between the acoustic pressure fluctuations and the unsteady flow-field through circular holes", *ASME Jnl. of Eng. For Gas Turbines & Power*, 132, pp 06150-1 -9, 2010.
21. Rupp, J., Carrotte, J.F., Spencer, A., "Methodology to identify the unsteady flowfield associated with the loss of acoustic energy in the vicinity of circular holes", ASME GT2010-22178, 2010.
22. Acharya, S., Baliga, B. R., Karki, K., Murthy, J. Y., Prakash, C., Vanka, S. P., "Pressure-based finite-volume methods in Computational Fluid Dynamics", *ASME Jnl. of Heat Transfer*, 129, pp 407-424, 2007.
23. Tam, C. K. W., Webb, J. C., "Dispersion relation preserving finite-difference schemes for computational acoustics", *Jnl. of Comp. Phys.*, 107, pp 262-281, 1993.
24. Bogey, C. and Bailly, C., "A family of flow dispersive and low dissipative explicit schemes for flow and noise computation", *Jnl. of Comp. Phys.*, 194, pp 194-214, 2004.
25. Shu, C. W., "Essentially non-oscillatory and weighted essentially non-oscillatory schemes for hyperbolic conservation laws", NASA ICASE Rep. No 97-65, 1997.
26. Shi, J., Hu, C., Shu, C. W., "A technique for treating negative weights in WENO schemes", *Jnl. of Comp. Phys*, 175, pp 108-127, 2002.
27. Tam, C. K. W., Hardin, J. C., "Second computational aeroacoustics workshop on benchmark problems", NASA CP-3352, 1997.
28. Dianat, M., Yang, Z., Jiang, D., McQuirk, J. J., "LES of scalar mixing in a coaxial confined jet", *Flow Turb. & Combustion*, 77, pp 205-227, 2006.
29. Foeller, S. and Polifke, W., "Determination of acoustic transfer matrices via Large Eddy Simulation and System Identification", AIAA 2010-3998, 16<sup>th</sup> AIAA/CEAS Aeroacoustics Conference, 7 - 9 Jun 2010 Stockholm.
30. Choi, D., Merkle, C. L., "Application of time iterative schemes to incompressible flow", *AIAA Jnl.*, 23, pp 1518-1524, 1985.
31. Choi, Y. H., Merkle, C. L., "The application of pre-conditioning in viscous flows", *Jnl. of Comp. Phys*, 105, pp 207-223, 1993.
32. McQuirk, J. J., Page, G. J., "Shock capturing using a pressure correction method", *AIAA Journal*, 27, pp 1751-1757, 1990.
33. Karki, K. C., Patankar, S. V., "Pressure based calculation procedure for viscous flows at all speeds in arbitrary configurations", *AIAA Journal*, 27, pp 1167-1173, 1989.
34. Demirdzic, U., Lilek, Z., Peric, M., "A collocated finite volume method for predicting flows at all speeds", *Int. Jnl. for Numerical methods in Fluids*, 16, pp1029-1050, 1993.
35. Hirsch, C., "Numerical computation of internal and external flows", Vol. 2, Wiley and Sons, 1990.
36. Colonius, T., "Modeling Artificial Boundary Conditions for compressible flow", *Annual Rev. of Fluid Mech.*, 36, pp 315-345, 2005.
37. Thompson K.W, Time-dependent boundary conditions for hyperbolic systems, *J Comp. Phys.* 68, pp 439-461, 1987.
38. Hedstrom G.W, Non-reflecting boundary conditions for nonlinear hyperbolic systems, *J. of Comp. Phys.*, 30, pp 222-237, 1979.
39. McQuirk, J., J., and Spencer, A., "Coupled and uncoupled CFD prediction of the characteristics of jets from combustor air admission ports", *ASME Jnl. of Eng. For Gas Turbines and Power*, 123, pp 327-332, 2001.
40. Denman, P. A., Barker, A. G., Jayatunga, C. W., McQuirk, J. J., "Modelling and measurements of combustor cooling tile flows", ASME GT-2003-38793, 2003
41. Ferziger, J. H., Peric, M., "Computational Methods for Fluid Dynamics", Springer Verlag, 1996.
42. Durbin, P. A., "On the k-ε stagnation point anomaly", *Int. Jnl. of Heat and Fluid Flow*, 17, pp 17-20, 1996.
43. Rhie, C.M., Chow, W.L., "Numerical study of the turbulent flow past an airfoil with trailing-edge separation", *AIAA Journal*, 21, 1983, pp 125-132.
44. Fischer, A., Bake, F., Roehle, I., "Broadband entropy noise phenomena in a gas turbine combustor", ASME GT2008-50263, 2008.
45. Gharib, M., Rambod, E., Shariff, K., "A universal time scale for vortex ring formation", *Jnl. of Fluid Mech.*, 360, pp 121-140, 1998.
46. Testud, P., Auregan, Y., Moussou, P., and Hirschberg, A., The whistling potentiality of an orifice in a confined flow using the energetic criterion, *J. Sound & Vib*, 325, pp 769-780, 2009.